


FULL PAPER

A numerical study of extensional flow-induced crystallization in filament stretching rheometry

Frank P. A. van Berlo  | Ruth Cardinaels  | Gerrit W. M. Peters  |
Patrick D. Anderson 

Polymer Technology, Department of Mechanical Engineering, Eindhoven University of Technology, The Netherlands

Correspondence

Patrick D. Anderson, Polymer Technology, Department of Mechanical Engineering, Eindhoven University of Technology, 5600 MB Eindhoven, Netherlands.
Email: p.d.anderson@tue.nl

Funding information

Eindhoven University of Technology

Abstract

A finite element model is presented to describe the flow, resulting stresses and crystallization in a filament stretching extensional rheometer (FiSER). This model incorporates nonlinear viscoelasticity, nonisothermal processes due to heat release originating from crystallization and viscous dissipation as well as the effect of crystallization on the rheological behavior. To apply a uniaxial extension with constant extension rate, the FiSER plate speed is continuously adjusted via a radius-based controller. The onset of crystallization during filament stretching is investigated in detail. Even before crystallization starts, the rheology of the material can change due to the effects of flow-induced nucleation on the relaxation times. Both nucleation and structure formation are found to be strongly dependent on temperature, strain rate and sample aspect ratio. The latter dependence is caused by a clear distribution of crystallinity over the radius of the filament, which is a result of the nonhomogeneous flow history in the FiSER. Therefore, this numerical model opens the possibility to a priori determine sample geometries resulting in a homogeneous crystallinity or to account for the nonhomogeneity.

KEYWORDS

filament stretching rheometer, flow-induced crystallization, isotactic polypropylene, nucleation, numerical simulation, viscoelasticity

1 | INTRODUCTION

During processing, polymers experience complex flows, which in general consist of both shear and extensional flow. Depending on the processing conditions, one or the other may dominate. These types of flows are known to facilitate crystallization of polymers through alignment and deformation of entangled tubes of constrained polymer chains.¹ Keller and Kolnaar² demonstrated that shish-kebab structures can be formed in elongational flows, while Eder and Janeschitz-Kriegl³ showed that their formation also occurs in shear flows with high enough viscoelastic stresses. Compared with shear, extension is much stronger to deform polymer chains and hence to facilitate crystallization.⁴

McHugh et al.⁵ were one of the first to find a qualitative relation between pure extensional flow and crystallization, using a four-roll mill. With birefringence and dichroism measurements on ultra-high-molecular-weight polyethylene (UHMWPE) it was shown that orientation increases with distance from the stagnation point. They suggested that flow orientation results in a viscoelastic molecular strain, which might control the process for enhancing crystallization. The last decades, multiple apparatus were developed to measure crystallization in uniaxial extensional flows. Studies performed by Blundell et al.⁶ showed that X-ray radiation enables in situ observation of oriented crystallization during drawing at fast rates comparable to industrial conditions. A PET sample was clamped between two jaws

This is an open access article under the terms of the Creative Commons Attribution License, which permits use, distribution and reproduction in any medium, provided the original work is properly cited.

© 2020 The Authors. *Polymer Crystallization* published by Wiley Periodicals LLC.

attached to stepper motors, which allowed fast uniaxial bi-directional drawing up to rates of 10s^{-1} . In situ wide-angle X-ray diffraction (WAXD) experiments were performed close to T_g . At low temperatures and high drawing rates, orientation is mainly in the drawing direction and independent of draw rate. At high temperatures and low drawing rates, no orientation was observed. The onset of crystallization was observed before the end of drawing and the strain-induced crystallization rate was found to be independent of temperature.⁶ In the work of Swartjes and Peters⁷ a cross-slit flow device was used to measure stress-induced crystallization in extensional flow using birefringence and WAXD measurements. The formation of highly oriented fiber-like crystal structures was demonstrated. Moreover, Janeschitz-Kriegl⁸ demonstrated through creep experiments with a pneumatically controlled filament stretching rheometer that extensional flow can enhance the rate of nucleation.

Hadinata et al.⁴ and Sentmanat et al.⁹ investigated the effect of flow-induced crystallization using a Sentmanat extensional rheometry add-on (SER). By means of ex situ differential scanning calorimetry (DSC) qualitative differences in the heat flow signatures were found for various temperatures, extension rates and strains, indicating an increase in crystallinity for stretched polybutene samples. Unfortunately, the study does not include any additional microscopy or small-angle X-ray scattering (SAXS) data. Hence, the evolution of crystal size and morphology with extension rate is not available.

A major challenge in extensional flow-induced crystallization measurements is applying a well-controlled extension rate, combined with a well-defined temperature protocol. For this reason Chellamuth et al.,¹⁰ used a filament stretching extensional rheometer (FiSER) with a custom-built oven, which is capable of imposing uniaxial extensional flow with a locally controlled constant rate while regulating temperature. In this FiSER flow is applied by placing a polymer sample between two pistons and moving the upper piston upwards. The extensional flow-induced crystallization is measured ex situ with DSC and SAXS over a broad range of extension rates and Hencky strains. In this study on polybutene it is suggested that the nucleation density may have already increased drastically even under moderate strains. Bischoff White et al.¹¹ performed similar ex situ crystallization measurements for isotactic polypropylene (iPP). The time required for the onset of crystallization was found to be linearly proportional to the inverse of extension rate, meaning that the onset of crystallization occurs at a constant strain value. This was true even for low extension rates where little polymer deformation is expected and where no increase in crystallinity from the quiescent state was found. They suggest that this might be the result of either polydispersity of the polymer or an increased interaction between undeformed polymers as they are advected by the imposed extensional flow. Also Wingstrand and van Drongelen¹² used a FiSER to characterize ex situ the crystallization characteristics of low-density polyethylene (LDPE) in extensional flow. An important finding in this work is that the structure orientation is determined by the backbone stretch instead of the global stretch.

To investigate crystallization kinetics of extensional flows in more detail in situ measurements are relevant.^{10,13} Therefore, Liu et al.¹⁴ developed a miniature SER to perform well-characterized uniaxial

extension with in-situ crystallization measurements using SAXS. With this SER, Wang et al.^{15,16} showed the chain-to-crystal network transition of iPP with a two-step experimental procedure and they captured the nonequilibrium structural and morphological behavior of poly(1-butene) in strain rate-temperature space (strain rates up to 33s^{-1}). However, in a SER, only the global extension rate is controlled due to which the local values may vary substantially.¹⁷ Therefore, recently, within our group, a FiSER design was realized wherein both pistons move at equal speed in opposite directions.¹⁸ As a result, a stagnation point is formed at the center of the filament, while ensuring a constant uniaxial extension rate with a radius-based controller. This makes it possible to measure the extensional rheological properties while in situ structure characterizations can be performed by means of X-ray scattering.¹⁸ Thereby, shish-kebab growth in LDPE was followed during extensional flow.

By combining experiments with numerical simulations, accurate rheological and structural data can be extracted, even when nonideal experimental parameters are present. The approach of coupling crystallization to deformation calculated with a rheological model on a continuum level was first presented by Zuidema et al.¹⁹ Their model was slightly modified by Steenbakkens et al.,²⁰ who replaced the recoverable strain as driving force for flow-induced nucleation and crystallization by backbone stretch, and predicted shish growth after a critical backbone stretch of the high molecular weight tail. However, van Erp et al.²¹ showed that a time integral over backbone stretch is a more realistic criteria. This approach is also used by van Drongelen et al.²² to model primary crystallization of linear low-density polyethylene (LLDPE). An in-depth evaluation of the flow-induced-crystallization (FIC) model developed in our group and parameterized for iPP, can be found in literature.^{19–21,23} A slightly different approach was used by Roozmond et al.,²⁴ since in their model, shish growth is linked to deformation rate and not to a critical backbone stretch. This numerical model captures both rheology and crystallization of iPP at high shear rates occurring in a nonhomogeneous slit flow. It shows good agreement with experimental data for crystallization over a very wide range of shear rates, pressures and temperatures.^{24,25} Grosso et al.²⁶ extended this model by using molecular considerations for setting the stretch relaxation times in the viscoelastic constitutive equation and the improved model can predict the formation of local complex structures of iPP in slit flows.²⁶ The continuum model of Grosso et al.²⁶ has been implemented in an in-house developed finite element package (TFEM) and will be used in this study after generalization of the flow type to include extension.

To study extensional flow-induced crystallization at very small to intermediate spatiotemporal scales molecular dynamics (MD) and multiscale modeling techniques are used respectively. These methods are complementary to the continuum approach discussed above because they provide molecular level details of the crystallization process. Nicholson and Ruthledge²⁷ were the first to use nonequilibrium MD simulations to study crystal nucleation and crystalline ordering under uniaxial extension. More recently, Zhao et al.²⁸ investigated the effect of molecular weight distributions (MWDs) on the formation of shish-kebabs in extensional flows by means of MD simulations. From this followed that broader MWDs have a positive effect on shish nuclei

formation, crystallization speed, and the generation of more regular, compacter, and thicker lamella, while final crystallinity is not affected by the MWD. Moreover, Sefiddashi et al.²⁹ used MD simulations to study flow-induced phenomena in entangled solutions of polyethylene dissolved in *n*-hexadecane and benzene solvents. The simulations revealed that the phases chemically separate at extension rates larger than the inverse of the Rouse time of the solution and that semi-crystalline domains form at large extension rates regardless of the solvent. Although MD simulations contribute to a mechanistic understanding of the structural changes during flow-induced crystallization, they have limitations in terms of length scales, MWDs and undercooling that can be reached. Hence, they cannot be used to directly model (FiSER) experiments. A promising multiscale simulation technique has been developed by Read et al.³⁰ They proposed a rapidly solvable multiscale model for FIC using a combination of MD and kinetic Monte Carlo simulations. However, this model is limited to single phased crystallization, while most polymers show polymorphic behavior. The finite element model developed within our group captures the interaction between rheology and crystallization and describes multi-phase parent-daughter structures on a large spatio-temporal scale, which are both needed to simulate FiSER experiments. Simulations of the flow in the FiSER are performed to study the extensional flow, structure formation, and resulting forces on the pistons. The rheology in the melt state and effects thereon caused by deviations from pure uniaxial extension in a FiSER will be the subject of another work, currently under preparation. Here, the main goal is to investigate the influence of experimental parameters on the flow-induced structure formation in order to understand the complexity of the FiSER experiment and to explore the best experimental conditions to get useful interpretable experimental results.

2 | MODELING

The extensional flow is created in a FiSER, by simultaneously moving the two pistons in opposite directions with equal velocities. To minimize the computational costs and taking into account axial symmetry, only a part of the FiSER is modeled, as shown in Figure 1. A cylindrical coordinate system will be used throughout this paper, with components (r, θ, z) and the origin is positioned at the middle of curve Γ_3 . Note that the negative z -direction is directed in the gravitation direction. The total computational domain of the FiSER is denoted by Ω . This computational domain is divided in two sub-domains Ω_1 and Ω_2 , where $\Omega = \Omega_1 \cup \Omega_2$, which are defined as the fluid sample and the pistons respectively. The shape of the fluid domain is determined by the radius of the piston R_p , the mid-radius $R(t)$ and the length of the filament $L(t)$. In FiSER experiments, the sample is slightly compressed after loading to a length L_c to ensure good contact with the plates. The aspect ratio of the compressed sample is then defined as $\Lambda_c = L_c/R_c$, with R_c the radius of the sample after compression. Here, it is assumed that the radius after compression R_c equals the piston radius R_p (see Table 1). In addition, a slow prestretch is used in experiments to increase the initial aspect ratio to $\Lambda_0 = L_0/R_0$, where R_0 is the mid-

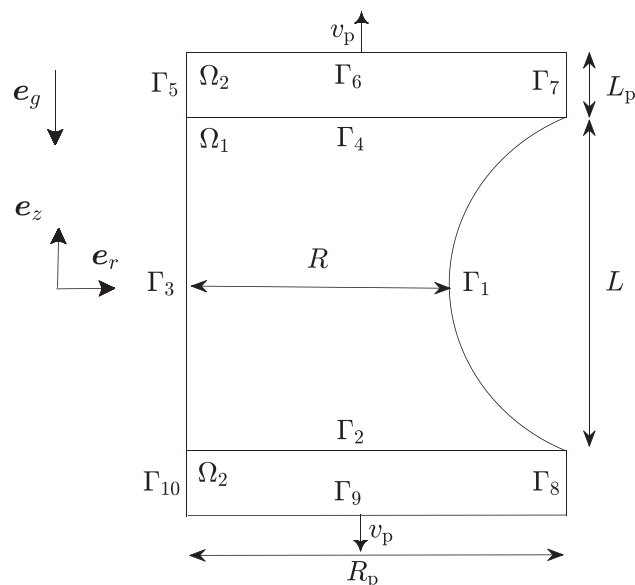


FIGURE 1 Initial axisymmetric geometry of a polymer sample (domain Ω_1) connected to two steel pistons (domain Ω_2). Boundaries Γ_3 , Γ_5 and Γ_{10} are positioned at $r = 0$ mm

radius of the sample after the prestretch. The simulations start after the prestretch. Then, the initial geometry of the filament is built, where the shape of the free surface Γ_1 is a circular or an ellipsoidal arc, whereby the latter is used when $(R_p - R_0) > L_0/2$. On Γ_3 axisymmetric boundary conditions are imposed. Subsequently, the pistons are simultaneously moved apart to a length $L(t)$ (with a velocity $v_p(t)$), in such a way that the middle of the sample is extended with a constant strain rate. The balance between surface tension, internal stresses, and gravity forces determines the shape of the free surface Γ_1 during extension. Because the crystallization, both in terms of crystal growth rate and structure formation, is dependent on temperature,²⁴ it is chosen to model both the co-moving pistons. This way, heat generated during crystallization in the polymer can be transferred to the pistons by means of conduction or can be convected to the surroundings at the free surface. The flow and crystallization equations are solved only on domain Ω_1 , while the energy equations are solved on the total domain Ω (i.e., Ω_1 and Ω_2).

The geometries used in this article are given in Table 1. The dimensions are chosen so that the effect of the compressed aspect ratio can be studied. Therefore, the amount of prestretch is equivalent for all geometries. The dimensions of the pistons used in the simulations are $L_p = 10$ mm and $R_p = R_c = 4$ mm.

The material used in this study is an iPP homopolymer (Borealis HD601CF, $M_w = 365$ kg/mol, and $M_n = 68$ kg/mol), which is characterized and examined in other studies.^{21,24,26,31} The material rheology is fitted with the XPP constitutive model. Note that two different sets of XPP parameters are reported in literature. The first set is given by Roozmond et al.³² Grosso et al.²⁶ modified these XPP parameters based on molecular considerations. In this paper the latter set is used. An overview of the used material parameters can be found in Appendix A.








N_{geo}	R_c (mm)	L_c (mm)	Λ_c	Compressed shape	R_0 (mm)	L_0 (mm)	Λ_0	Initial shape
1	4.0	1.1	0.3		1.68	3.64	2.17	
2	4.0	2.1	0.5		1.68	6.0	3.57	
3	4.0	3.8	1.0		1.68	10.0	5.92	
4	4.0	5.9	1.5		1.68	15.0	8.92	

TABLE 1 Overview of the geometries studied with the crystallization model. The dimensions of the compressed and prestretched state are given

Note: Simulations start from the (prestretched) initial shape, at a prestrain of $\varepsilon_{\text{pre}} = 1.74$.

2.1 | Flow equations

To solve the flow in the filament stretching rheometer, the momentum and mass balance have to be solved. The following equations are used assuming an incompressible fluid:

$$\rho \frac{D\mathbf{u}}{Dt} = -\nabla p + \nabla \cdot \boldsymbol{\tau} + \nabla \cdot (2\eta_s \mathbf{D}) + \rho g \mathbf{e}_g \quad \text{in } \Omega_1, \quad (1)$$

$$\nabla \cdot \mathbf{u} = 0 \quad \text{in } \Omega_1, \quad (2)$$

where \mathbf{u} is the fluid velocity, ρ the density of the material, p the pressure, \mathbf{D} the deformation rate tensor and the extra stress tensor is defined by $\boldsymbol{\tau}$. A relatively small viscous component η_s is added for numerical reasons and g and \mathbf{e}_g are the magnitude and direction of gravity, respectively. The extra stress tensor is given by:

$$\boldsymbol{\tau} = \sum_i^{N_{\text{modes}}} g_i (\mathbf{c}_i - I). \quad (3)$$

Here, \mathbf{c}_i is the conformation tensor of mode i and g_i is the modulus of mode i , which equals η_i/λ_i . Here, η_i is the viscosity and λ_i the relaxation time of mode i and N_{modes} the amount of modes. The constitutive model used for predicting the conformation tensor is the multi-mode XPP model.³³ Originally, the XPP model was proposed for branched polymers, but it also captures the physics of linear polymers, as shown by Verbeeten et al.³⁴ for high-density polyethylene (HDPE). The differential equation of the XPP model is given by:

$$\nabla \mathbf{c}_i + 2 \frac{\exp[\nu_i (\sqrt{\text{tr} \mathbf{c}_i} - 1)]}{\lambda_{s,i}} \left(1 - \frac{3}{\text{tr} \mathbf{c}_i} \right) \mathbf{c}_i + \frac{1}{\lambda_{b,i}} \left(\frac{3\mathbf{c}_i}{\text{tr} \mathbf{c}_i} - I \right) = \mathbf{0}, \quad (4)$$

where $\nabla \mathbf{c}_i$ is the upper convected derivative of the conformation tensor, $\lambda_{b,i}$ the relaxation time for backbone tube orientation, $\lambda_{s,i}$ the backbone stretch relaxation time and the parameter ν_i depends on the number of arms of the molecule q_i following $\nu_i = 2/q_i$.³³ Note that for nonbranched polymers q_i is a fitting parameter. For the crystallization model, the backbone molecular stretch, Λ_i , is a commonly used

measure for driving flow-induced nucleation. This backbone stretch is defined as:

$$\Lambda_i = \sqrt{\text{tr} \mathbf{c}_i / 3}. \quad (5)$$

The relaxation spectra and nonlinear parameters of the XPP model are given in Table A.1 in Appendix A.

2.2 | Energy balance

The crystallization process, both in terms of crystal growth rate and structure formation, is strongly dependent on temperature.²⁴ To find the temperature in the filament, the following energy balance is solved:

$$\rho c_p \frac{DT}{Dt} = k \nabla^2 T + \rho \chi_\infty \Delta H \dot{\xi} + \boldsymbol{\sigma} : \mathbf{D} \quad \text{in } \Omega_1, \quad (6)$$

where ρ is the density, T the temperature, c_p the specific heat capacity at constant pressure, k the thermal conductivity coefficient, ΔH the heat of fusion, χ_∞ the total crystallinity of the equilibrium state ($t = \infty$), ξ the space filling and $\boldsymbol{\sigma} = \boldsymbol{\tau} - pI$ the total stress tensor. In this heat balance, heat conduction, latent heat release due to crystallization and viscous dissipation are taken into account in respectively the first, second and third term on the right-hand side. It is assumed that the ρ , c_p and k do not change with temperature or during phase transitions from the molten to the crystalline state.

In the energy balance of the steel pistons, heat generation due to crystallization and viscous dissipation is not present. Therefore, Equation (6) reduces to

$$\rho_s c_{p,s} \frac{DT}{Dt} = k_s \nabla^2 T \quad \text{in } \Omega_2, \quad (7)$$

for the steel pistons. Here, the subscript s is used to indicate that the parameters apply to the steel pistons. Values of the parameters in both energy equations are presented in Table A.2 in Appendix A.

2.3 | Quiescent crystallization

Rozepond et al.²⁴ proposed a nonisothermal crystallization model that is based on the Kolmogoroff-Avrami expression. Space filling by crystallization is given by

$$\xi(t) = \frac{\chi(t)}{\chi_\infty} = 1 - \exp\{-\Phi_0(t)\}, \quad (8)$$

where χ is the crystallinity at time t . The crystal volume Φ_0 represents the sum of the undisturbed crystallized volumes of the different phases, $\Phi_0 = \sum \Phi_{0,i}(t)$. The subscript i indicates the phases of a multi-phase system (α -, β -, γ -phases for iPP). For nonisothermal crystallization of spherulites, the crystal volumes (i.e., when crystal structures can grow without taking into account impingement) $\Phi_{0,i}$ can be described by the Schneider rate equations,³⁵ a set of differential equations, which describe the structure development for quiescent conditions. The local mean number of spherulites and their mean radius, surface and volume are calculated as follows:

$$\dot{\Phi}_{3,i} = 8\pi\dot{N}_i \quad (\Phi_3 = 8\pi N) \text{ 'rate'}. \quad (9)$$

$$\dot{\Phi}_{2,i} = G_i\Phi_{3,i} \quad (\Phi_2 = 8\pi R_{\text{tot}}) \text{ 'radius'}. \quad (10)$$

$$\dot{\Phi}_{1,i} = G_i\Phi_{2,i} \quad (\Phi_1 = S_{\text{tot}}) \text{ 'surface'}. \quad (11)$$

$$\dot{\Phi}_{0,i} = G_i\Phi_{1,i} \quad (\Phi_0 = V_{\text{tot}}) \text{ 'volume'}. \quad (12)$$

with the nucleation density N , the nucleation rate \dot{N} and the growth rate G . The growth rate is captured by the following quadratic exponential function²⁴:

$$G_i(T) = G_{\text{max},i,0} \exp\left\{-c_{G,i}(T(t) - T_{G,\text{ref},i,0})^2\right\}. \quad (13)$$

Here, $G_{\text{max},i}$ is the growth rate at the reference temperature $T_{G,\text{ref},i}$ and $c_{G,i}$ a constant. The nucleation density, for heterogeneous nucleation is given by the linear exponential function:

$$\frac{dN_q}{dT} = -c_N N_{\text{ref}} \exp\{-c_N(T(t) - T_{N,\text{ref}})\}. \quad (14)$$

Here, the subscript q is used to define quiescent parameters, N_{ref} is the number of nuclei evaluated at the reference temperature $T_{N,\text{ref}}$ and c_N is a constant. During solidification in a multi-phase system, every crystal phase i generates a crystal volume fraction, $\Phi_{0,i}$, using a share of the available number of nuclei and having its own growth rate. The ratio by which the nuclei are divided between the crystal phases is not accessible experimentally. Therefore, the assumption is made that the allocation of nuclei to a given crystal form scales with the ratio of the individual crystal phase growth rates at the current temperature and pressure.²² For isobaric conditions, the nucleation rate for a given crystal form is given by:

$$\dot{N}_{i,q} = f_{i,q} \frac{dN_q}{dT}, \quad (15)$$

with the quiescent growth rate weighted fraction, $f_{i,q}$, defined as:

$$f_{i,q} = \frac{G_i}{\sum G_i}. \quad (16)$$

In the paper of Rozepond et al.,²⁴ the α -, β - and γ -phases of iPP are modeled. Since the β -phase only forms during flow, the quiescent growth rate weighted fraction $f_{i,q}$ is restricted to $i = \alpha, \gamma$ and $f_{\beta,q} = 0$. With the nucleation density and individual growth rates modified for nonisothermal and isobaric conditions, the rate of space filling in a multi-phase structure is calculated as a function of time using:

$$\dot{\xi}_i(t) = (1 - \xi(t))\dot{\Phi}_{0,i}. \quad (17)$$

Values of the parameters used in the quiescent crystallization model can be found in Table A.4 in Appendix A.

2.4 | Flow-induced nucleation and crystallization

In the presence of flow, the total number of nuclei is the sum of the quiescent nuclei, N_q and the nuclei originating from FIC, N_f :

$$\dot{N}_{i,\text{tot}} = \dot{N}_{i,q} + f_{i,f}\dot{N}_f, \quad (18)$$

where $\dot{N}_{i,q}$ follows from Equation (15). The total amount of nuclei is used in the Schneider rate Equation (9). The flow enhanced nucleation rate is assumed to depend via an exponential relation on the backbone stretch of the high-molecular weight mode. This leads to²⁴:

$$\dot{N}_f = g_n(T) \exp\{\mu_n(\Lambda_{\text{HMW}}^2 - 1)\}. \quad (19)$$

Here, Λ_{HMW} is the high molecular weight stretch calculated according to (5), using the conformation tensor \mathbf{c}_{HMW} , which is the conformation tensor with the longest relaxation time in the XPP model, and μ_n and g_n are scaling parameters. The scaling parameter g_n depends on temperature as follows:

$$g_n(T) = g_{n,\text{ref}} 10^{c_{n,T}(T - T_{\text{ref}})}. \quad (20)$$

Here, $c_{n,T}$ is a fitting parameter and $g_{n,\text{ref}}$ and T_{ref} are the reference scaling parameter and temperature, respectively. For iPP in flow, the growth rate weighted functions (given in Equation (16)) are different, because of the possibility to grow β -phase crystals. The growth rate weighted functions in flow are defined as²⁴:

$$f_{\alpha,f} = (1 - f_{\beta,f}) \frac{G_\alpha}{G_\alpha + G_\gamma}, \quad (21)$$

$$f_{\gamma,f} = (1 - f_{\beta,f}) \frac{G_\gamma}{G_\alpha + G_\gamma}, \quad (22)$$

$$f_{\beta,f} = f_{\beta}. \quad (23)$$

Here, f_{β} is a relatively small number (see Table A.4 in Appendix A), because only a small amount of β -phase is formed during flow compared to α - and γ -phase.

The growth mechanism of oriented structures (shish) is based on the “streamers” concept introduced by the Kornfield group.³⁶ Shish propagate in the lengthwise direction by addition of chain segments with length ξ_{seg} . Furthermore, it is assumed that the material around a shish tip deforms affinely. The expression for the lengthwise propagation of shish then becomes:

$$\dot{L} = \dot{\gamma} \xi_{\text{seg}}. \quad (24)$$

Here, L is the shish length, $\dot{\gamma}$ the shear rate and ξ_{seg} is on the order of the chain segment length. The lengthwise propagation of shish in iPP is modeled as a dependency on the shear rate. To support extensional flows, the shear rate in this equation is replaced with the magnitude of the rate of deformation tensor \mathbf{D} :

$$\dot{\gamma} = \dot{\gamma}_{\text{eff}} = \sqrt{2\mathbf{D} : \mathbf{D}}. \quad (25)$$

In case of (pure) uniaxial extension with extension rate $\dot{\epsilon}$, the effective strain rate becomes $\dot{\gamma}_{\text{eff}} = \sqrt{3}\dot{\epsilon}$. Since it is assumed that the nucleation sites grow in the lengthwise direction, the specific shish length growth \dot{L}_{tot} is expressed as:

$$\dot{L}_{\text{tot}} = 2N_f \dot{L}, \quad (26)$$

For the current model, no critical flow condition is used for the formation of shish. However, appropriate shish formation is captured with the model, because nucleation rate \dot{N}_f and propagation rate \dot{L} are low for weak to mild flows.

The undisturbed volume can be calculated from the calculated shish length and nucleation density. The crystalline volume fraction from the kebabs growing on shish is determined with rate equations. It is assumed that kebabs form on both the α - and γ -phase:

$$\dot{\Psi}_{1,\alpha} = 4\pi G_{\alpha,p} L_{\text{tot}} \frac{G_{\alpha,p}}{G_{\alpha,p} + G_{\gamma}}, \quad (27)$$

$$\dot{\Psi}_{1,\gamma} = 4\pi G_{\gamma,p} L_{\text{tot}} \frac{G_{\gamma}}{G_{\alpha,p} + G_{\gamma}}. \quad (28)$$

Here, Ψ_1 is a measure for the surface area of kebabs. On α -kebabs, three different crystal morphologies can nucleate: α -parents, α -daughters and γ -daughters. It is assumed that on γ -kebabs, only γ -phase can grow. These conditions are mathematically expressed as follows:

$$\dot{\Psi}_{0,\alpha,p} = G_{\alpha,p} \Psi_{1,\alpha} \frac{G_{\alpha,p}}{G_{\alpha,p} + G_{\alpha,d} + G_{\gamma}}, \quad (29)$$

$$\dot{\Psi}_{0,\alpha,d} = G_{\alpha,d} \Psi_{1,\alpha} \frac{G_{\alpha,d}}{G_{\alpha,p} + G_{\alpha,d} + G_{\gamma}}, \quad (30)$$

$$\dot{\Psi}_{0,\gamma,p} = G_{\gamma} \Psi_{1,\gamma}, \quad (31)$$

$$\dot{\Psi}_{0,\gamma,d} = G_{\gamma} \Psi_{1,\alpha} \frac{G_{\gamma}}{G_{\alpha,p} + G_{\alpha,d} + G_{\gamma}}. \quad (32)$$

Here, Ψ_0 is a measure for the undisturbed volume of kebabs and subscripts p and d denote the volumes in parent crystals or daughter crystals, respectively. The total volume of kebabs is much larger than the volume of shish and therefore the volume of shish is neglected.

Roozmond et al.³² suggest that flow and the following relaxation afterwards increase the growth of kebabs. This phenomenon is accounted for by increasing the growth rates of the α -parents with a factor G_{flow} . It is assumed that only for α -parents the growth rate increases due to orientation. The growth rate of the other two morphologies is always equal to the growth rate in quiescent conditions.²⁶ After flow, this effect relaxes due to relaxation of the chains towards their equilibrium conformation. Grosso et al.²⁶ introduce a direct relation between the α -parent growth rate and the molecular conformation. The expression for the growth rate of α -parents is given by²⁶:

$$G_{\alpha,p}(T, t) = G_{\alpha}(T) (1 + G_{\text{flow}} \exp\{\text{tr}(c_{\text{HMM}})\}). \quad (33)$$

This way, during flow the growth rate of α -parents is more pronounced and this effect reduces afterwards because of the relaxation of the conformation tensor. The formation of the daughter morphology is less preferable because of the flow-induced conformation. However, because the growth of daughter crystals only becomes noticeable after relaxation of the conformation, the growth rate for α -daughters equals the quiescent growth rate:

$$G_{\alpha,d}(T, t) = G_{\alpha}(T). \quad (34)$$

To take into account the impingement of the shish-kebab structures, the expressions for the space filling in Equation (8) and (17) have to be adjusted. The total space filling and the space filling rate of each individual phase are given by:

$$\xi_{\text{tot}} = 1 - \exp\left[-\sum_{i,j} (\Phi_{0,i} + \Psi_{0,i,j})\right], \quad (35)$$

$$\dot{\xi}_i = (1 - \xi_{\text{tot}}) \left(\dot{\Phi}_{0,i} + \sum_j \dot{\Psi}_{0,i,j} \right), \quad (36)$$

with the phase $i = \alpha, \gamma$ and the morphology $j = d, p$ (daughter or parent). The total space filling, ξ_{tot} , reaches 1 when the crystallization process is completed. Parameters for the flow-induced crystallization are given in Table A.4 in Appendix A.

2.5 | Effects on the rheology

Roosmond et al.²⁴ have shown that shish strongly influence the rheology of the melt, even before the crystalline volume is considerably large.²⁴ It is hypothesized that chains protruding from shish into the melt influence the rheology on a macroscopic scale. In the model of Roosmond et al.²⁴ this is implemented in an empirical way by defining the effect of crystallization on the modulus as:

$$g_i = g_{0,i} \mu 10^{v_{\text{eff}}}, \quad (37)$$

wherein $g_{0,i}$ is the modulus of mode i , μ is the ratio between the modulus of the crystal and the one of the melt and v_{eff} is the effective space filling of shish-kebabs, given by;

$$v_{\text{eff}} = 1 - \exp\{-\pi L_{\text{tot}} r_{\text{eff}}^2\}, \quad (38)$$

where r_{eff} is the effective radius of a shish. Because this approach contains a number of uncertainties, the shish radius is an adjustable parameter on the order of 35 nm for iPP.²⁴ The effective shish radius and the modulus ratio between crystal and melt are set to $r_{\text{eff}} = 30$ nm and $\mu = 5$.²⁶

Housmans et al.³¹ modeled the reputation time and the Rouse time as linear functions of the amount of flow-induced nuclei (i.e., number density of flow-induced nuclei). The flow-induced nuclei are assumed to act as physical cross-links in the melt and these cross-links increase the relaxation times of the high molecular weight chains. Following their approach, a dependence of the Rouse time on the amount of flow-induced nuclei is proposed:

$$\lambda_{s,j} = \lambda_{s,i_0} a_T (1 + \alpha_s N_f), \quad (39)$$

where λ_{s,i_0} are the stretch relaxation times at a reference temperature T_{ref} . Here, a value of $\alpha_s = 10^{-4} \text{ mm}^3$ is derived by Grosso et al. for the used iPP.²⁶ The temperature shift factor is defined as:

$$a_T = \exp\left[\frac{E_a}{8.31} \left(\frac{1}{T} - \frac{1}{T_{\text{ref}}}\right)\right], \quad (40)$$

with E_a the activation energy and T_{ref} the reference temperature. All parameters of previous equations are given in Table A.4 in Appendix A.

2.6 | Boundary and initial conditions

The polymer is at rest at the start of the simulation. Since a time derivative appears in Equation (4) for the viscoelastic fluid, an initial condition is needed for the conformation tensor c :

$$c(0) = I, \quad (41)$$

which means that the viscoelastic extra stress is initially assumed to be zero. Nonisothermal experiments are considered, wherein the

temperature is initially constant in the entire domain Ω , that is, $T(0) = T_0$ for all x . The temperature of the environment is assumed to be constant $T_{\infty} = T_0$ during the simulation. The initial number of quiescent nuclei is calculated via Equation (15). Since the model is polymorph, the initial number of quiescent nuclei per phase is defined as:

$$N_{q,i}(T_0) = f_{i,q} N_q(T_0), \quad (42)$$

where the growth rate weighted fraction, $f_{i,q}$, follows from Equation (16). The required growth rates per phase are also calculated by using the initial temperature, T_0 . Since initially no flow is applied, the number of flow-induced nuclei, the space filling and shish growth parameters are zero. However, these values cannot be set to zero, because the Schneider rate equations are solved logarithmically for stability purposes. Therefore, they are set to a small initial value of 10^{-6} .

To solve the governing equations, a set of boundary conditions has to be applied. In sub-domain Ω_1 , the velocities are prescribed as:

- $u_r = 0$ on Γ_2, Γ_3 and Γ_4 ,
- $u_z = -v_p$ on Γ_2 and $u_z = v_p$ on Γ_4 .
- $\mathbf{u} \cdot \mathbf{n} = 0$ on Γ_1 ,

where \mathbf{n} is the outward pointing normal vector on the surface S . On this boundary, the surface tension $\hat{\gamma}$ is applied using a Neumann boundary condition:

- $(-\rho \mathbf{l} + 2\eta_s \mathbf{D} + \boldsymbol{\tau}) \cdot \mathbf{n} = \nabla_s \cdot (\hat{\gamma}(\mathbf{l} - \mathbf{nn}))$ on Γ_1 ,

with ∇_s the surface gradient operator. A constant surface tension $\hat{\gamma}$ is assumed.

The energy equations are solved on the total domain Ω . Therefore, boundary conditions for the temperature are applied at both the filament and the pistons. The filament and pistons are subjected to heat losses at the free surface due to convection. Therefore, the following boundary condition is prescribed:

- $-k \nabla T \cdot \mathbf{n} = h(T - T_{\infty})$, on Γ_1, Γ_7 and Γ_8 ,

with h the convective heat transfer coefficient and $T_{\infty}(=T_0)$ the ambient temperature. The used convective heat transfer coefficient for the polymer is assumed to be $h = 79 \text{ W m}^{-2} \text{ K}^{-1}$. The temperature at the end of the pistons is assumed to be constant. Therefore, the following boundary condition is applied:

- $T = T_0$, on Γ_6 and Γ_9 .

All values of the parameters used in the boundary conditions can be found in Table A.3 in Appendix A.

3 | NUMERICAL METHODS

A finite element method is used to solve the filament stretching flow problem. The initial geometry is built with Gmsh.³⁷ For the velocity and pressure, isoparametric, triangular P_2P_1 (Taylor-Hood) elements are used, whereas for the conformation, temperature and crystallization evolution triangular P_1 elements are used. So, to solve the weak forms of the balance of mass, momentum and heat, second-order elements for the velocity are used, while first-order elements are used for the pressure, temperature and the conformation tensor.

More information about the weak forms can be found in prior works from our group.^{38,39} In order to solve these governing equations, the log-conformation representation,⁴⁰ streamline-upwind Petrov-Galerkin (SUPG),⁴¹ and DEVSS-G⁴² are used for stability. A logarithmic version of the crystallization evolution is used for numerical stability reasons.

3.1 | Mesh movement

The boundary which describes the free surface will move in time and also the boundaries connected to the pistons move. Therefore, it is necessary to track these boundaries and update the mesh on domain Ω_1 . The elements of the piston in domain Ω_2 do not change over time. The position change of the free surface is determined from the velocity at this boundary (Lagrangian based). The movement of the mesh has to be compensated. To do so, the Arbitrary Lagrangian Eulerian (ALE) formulation is used.⁴³ In this formulation the mesh velocity, \mathbf{u}_m is subtracted from the velocity \mathbf{u} to correct for the movement of the mesh. More details about the implementation of ALE in the numerical model of the FiSER is given elsewhere.^{43,44}

3.2 | Time integration

The system of equations is solved sequentially per time step. To integrate in time, a (semi-implicit) backward Euler scheme is employed for the first time step and a second-order backward differencing scheme (semi-implicit Gear⁴⁵) is employed for all subsequent time steps. The system of equations on the moving domain Ω are solved using the following steps:

First, the velocity, conformation, temperature and crystallization parameters are predicted from previous time steps using:

$$\hat{\mathbf{u}}^{n+1} = \mathbf{u}^n. \quad (43)$$

$$\hat{\mathbf{c}}^{n+1} = \mathbf{c}^n. \quad (44)$$

$$\hat{T}^{n+1} = T^n. \quad (45)$$

$$\tilde{Q}^{n+1} = \tilde{Q}^n. \quad (46)$$

for the first time step, and:

$$\hat{\mathbf{u}}^{n+1} = 2\mathbf{u}^n - \mathbf{u}^{n-1}. \quad (47)$$

$$\hat{\mathbf{c}}^{n+1} = 2\mathbf{c}^n - \mathbf{c}^{n-1}. \quad (48)$$

$$\hat{T}^{n+1} = 2T^n - T^{n-1}. \quad (49)$$

$$\tilde{Q}^{n+1} = 2\tilde{Q}^n - \tilde{Q}^{n-1}. \quad (50)$$

for all subsequent time steps. Here, the predictions of the velocity, conformation tensor, temperature and crystallization parameters for time t^{n+1} , t^n and t^{n-1} are given by $\hat{\mathbf{u}}^{n+1}$, $\hat{\mathbf{c}}^{n+1}$, \hat{T}^{n+1} , \tilde{Q}^{n+1} , \mathbf{u}^n , \mathbf{c}^n , T^n , \tilde{Q}^n , \mathbf{u}^{n-1} , \mathbf{c}^{n-1} , T^{n-1} and \tilde{Q}^{n-1} , respectively.

Second, the predictions of the temperature \hat{T}^{n+1} and crystallization parameters \tilde{Q}^{n+1} are used to determine the viscosities (moduli), backbone relaxation times and stretch relaxation times of each mode. These parameters are then used as input for the flow problem. The predicted temperature and crystallization dependent on viscosity (moduli) and relaxation times. These will be used for solving the velocity, pressure and the conformation tensor using the mass balance, the momentum balance and the constitute equation. Details about the solution for velocity, pressure and conformation procedure can be found elsewhere.³⁸

Using the current velocity field \mathbf{u}^{n+1} and the conformation tensor \mathbf{c}^{n+1} the crystallization evolution is solved. To do so, the entire crystallization variable array \tilde{Q} has to be solved, which consist out of 30 components (i.e., fields). Examples of fields in the crystallization array are the amount of nuclei, the growth rate, the Schneider rate components for quiescent and flow-induced crystallization and the space filling. Subsequently, the current crystallization variables \tilde{Q}^{n+1} , the velocity \mathbf{u}^{n+1} and the conformation tensor \mathbf{c}^{n+1} are used as an input for the energy balance. So, the temperature field T^{n+1} is solved using the weak form of the energy balance. Thereafter, T^{n-1} is filled with the previous solution T^n and the new temperature field T^{n+1} is copied to T^n . Also the velocity, conformation and crystallization parameters are copied in the same manner.

Finally, the boundary positions are updated, where the movement of the boundary is Lagrangian based using a backward Euler scheme:

$$\mathbf{x}_\Gamma^{n+1} = \mathbf{x}_\Gamma^n + \mathbf{u}^{n+1}(\Gamma)\Delta t, \quad (51)$$

where \mathbf{x}_Γ is the position of the boundary and Δt the time step. The coordinates of the mesh of the pistons are updated so that they follow the movement of boundaries Γ_2 and Γ_4 . The mesh velocities can now be obtained by numerically differentiating the mesh coordinates of domain Ω_1 . The mesh velocity is obtained in each node using a first-order backward differencing scheme⁴⁴:

$$\mathbf{u}_m^{n+1} = \frac{\mathbf{x}_m^{n+1} - \mathbf{x}_m^n}{\Delta t}, \quad (52)$$

where \mathbf{x}_m are the nodal positions of the mesh.

Due to the movement of the boundary, elements may become too deformed. Then a new mesh is generated and the current solution is projected on the new mesh. Besides the current mesh, also the previous mesh is remeshed, so that not only solutions n can be projected, but also solutions $n - 1$. This is necessary because a second-order time stepping scheme is used. The procedure of remeshing and the projection is explained in prior work.⁴⁴

3.3 | Implementation of the rheological and crystallization characterization

The implementation of the rheological characterization will be reported in another work, currently under preparation. This includes the calculation of the force and extensional viscosity, the radius of the filament, the strain rate controller, and the determination of the shear correction factor with the numerical simulations. During in situ X-ray measurements, an X-ray beam is sent through the middle of the filament. The obtained crystallinity is then an “average” over the mid-radius of the filament. To mimic this procedure, a method has been developed to calculate the average crystallinity over the radius of the sample. In the simulations, the total percentage of crystallinity is integrated over the dimensionless radius, $r^* = r/R_0$, according to:

$$\langle \chi_{\text{tot}} \rangle(t) = \int_0^1 \chi_{\text{tot}}(t, r^*) dr^*, \quad (53)$$

where $\langle \chi_{\text{tot}} \rangle$ is the total average crystallinity over the mid-radius of the filament.

The filament is extended with a constant strain rate during the simulations. As a result, the mid-radius of the filament decreases exponentially. For flow-induced crystallization to take place a large extension is needed and therefore the radius becomes very small. In order to make this computationally feasible, at large strains only five elements can be used in the radial direction at the middle of the filament. So at large strains, the amount of crystallization data acquired from the middle of the filament is limited. Therefore, it is chosen not to use the mid-line, but a mid-region to process the data from the simulations (see Figure 2). This way, more elements are included, resulting in more radial data points. A width of 100 μm of this mid-region is assumed to be comparable to the width of an actual X-ray beam.

4 | RESULTS AND DISCUSSION

In the first part of this section, the first geometry in Table 1 is studied to show the effect of nucleation on the rheological properties. Subsequently, the crystal growth is investigated for this sample at multiple temperatures and strain rates. This gives a clear overview of the effect

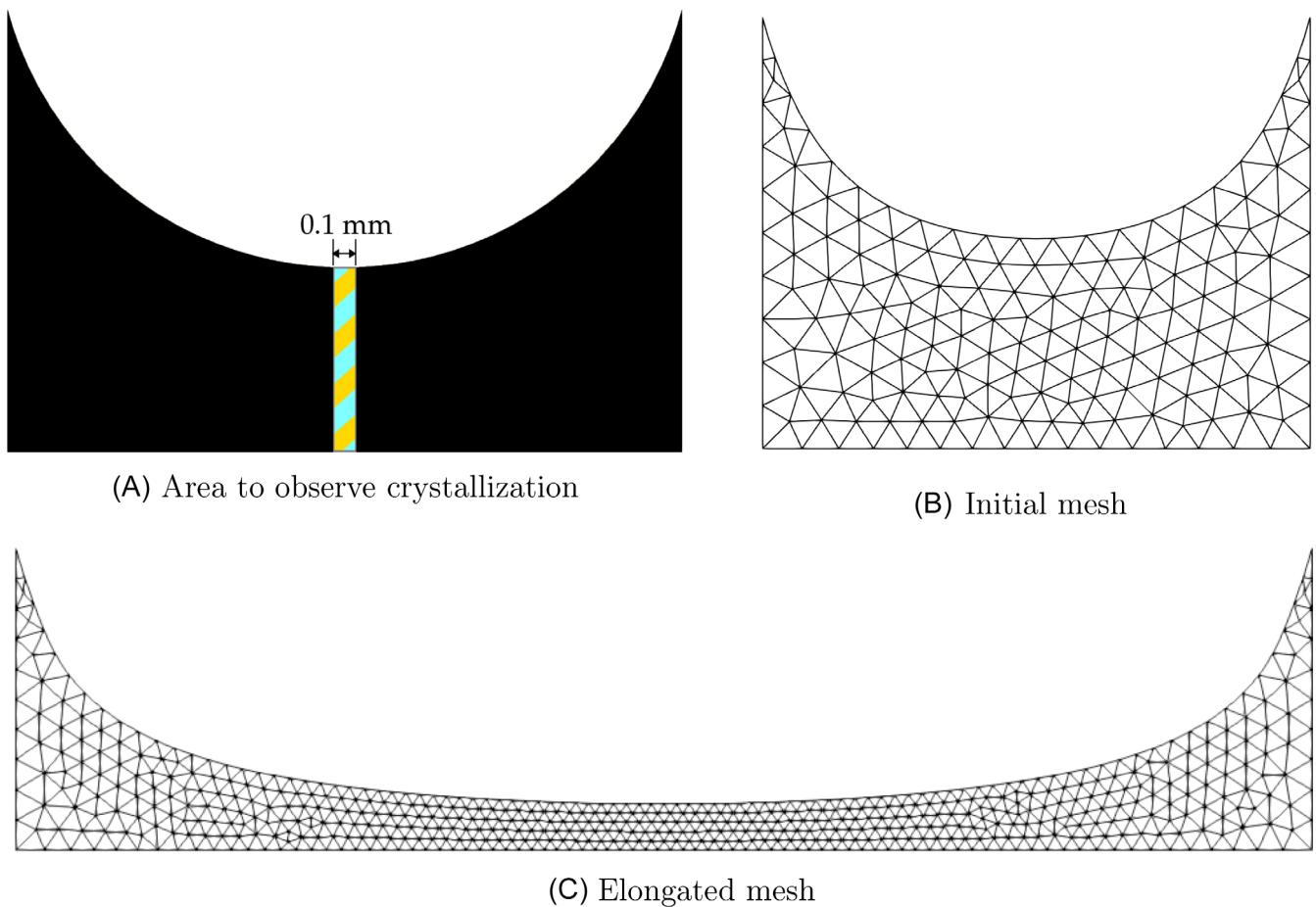


FIGURE 2 (a) Geometry of a filament with a marked mid-region. The mid-region of 0.1 mm is used to increase the amount of elements to obtain crystallization data and mimics the width of an X-ray beam. (b) and (c) examples of an initial and elongated mesh

of experimental conditions on the crystallization in the FiSER. At last, the effect of the compressed aspect ratio on the crystallization is studied.

4.1 | Effect of crystallization on the extensional viscosity

To investigate crystallization of iPP in the FiSER, geometry one in Table 1 is chosen. In the simulations, a strain rate of 10 s^{-1} and a temperature of 140°C are applied. At this temperature, the quiescent crystallization is negligibly small. The result of the extensional viscosity is shown in Figure 3. The pure uniaxial extensional solution, $\bar{\eta}_{\text{XPP}}^+$, is found by solving the XPP equations using a pure uniaxial extensional flow. In Figure 3 it can be seen that the simulated extensional viscosity matches this solution up to large strains. However, including the crystallization model results in a deviation at large strains. This is a result of flow-induced nucleation and enhanced growth. It is interesting to see that the deviation starts at a strain of approximately 3.8, while no crystallization is observed up until a strain of 4.5. When crystallization starts, the extensional viscosity rapidly increases. The primary increase in extensional viscosity (before crystallization) can be explained by the occurrence of flow-induced nuclei due to the stretch

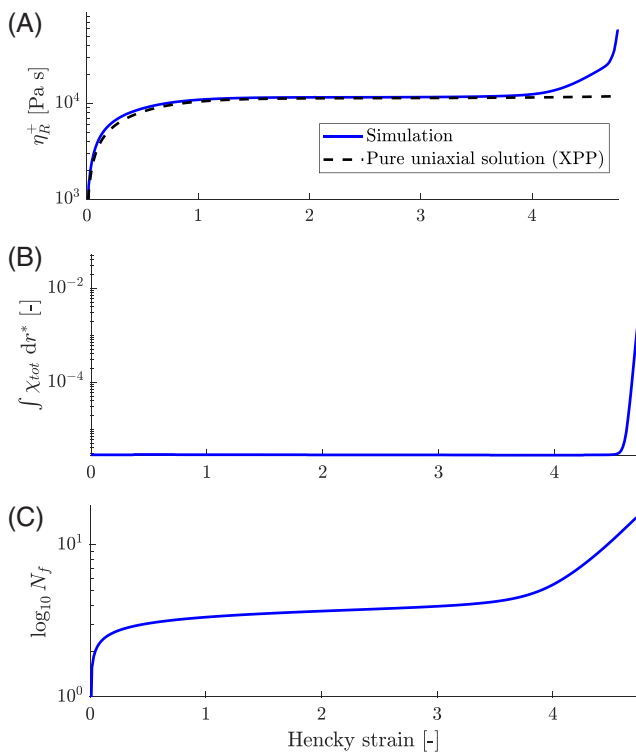


FIGURE 3 (a) Simulated extensional viscosity. The dashed line is the pure uniaxial solution calculated with the XPP model. (b) Corresponding crystal fraction integrated over the radius and (c) flow-induced nuclei at the free surface ($z = 0 \text{ mm}$). The compressed aspect ratio, strain rate and initial temperature are $\Lambda_c = 0.29$, $\dot{\epsilon} = 10 \text{ s}^{-1}$ and $T_0 = 140^\circ\text{C}$

of the high molecular weight tail. The flow-induced nuclei are assumed to act as physical cross-links in the melt and these cross-links increase the Rouse relaxation time of the high molecular weight chains according to Equation (39).³¹ Therefore, the extensional viscosity increases. It should be noted that the relaxation times are only slightly affected by temperature changes, because the temperature only increases with 0.2°C during stretching and crystallization ($\epsilon_H < 4.5$). The secondary, steep increase in the extensional viscosity is observed because flow-induced crystals grow, which significantly increases the moduli of the polymer, as given by Equation (37).

Surprisingly, the crystallinity is not constant over the mid-radius of the sample. Hence 1D modeling like often done for drops and films is not an option. At the center, the crystallinity is much lower than close to the free surface. The crystallization distribution for the geometry with a compressed aspect ratio of 0.29 is shown in Figure 4. Crystallinity is mainly located in a narrow region along the free surface.

To explain the crystallization distribution over the radius, the period before crystallization is studied. The important parameters for the onset of flow-induced crystallization are visualized at the center of the sample ($r = 0 \text{ mm}$) and at the free surface ($r = R_0$) in Figure 5. Starting with the magnitude of the rate of deformation tensor, $\dot{\gamma}_{\text{eff}}$, it can be seen that at the start the flow field is nonuniform. This results in a distribution of the trace of the conformation tensor and thus the high molecular weight stretch, Λ_{HMW} . This is because the sample is extended with a higher strain rate at the free surface than at the center of the sample ($\dot{\epsilon}_{\text{eff}} = \dot{\gamma}_{\text{eff}}/\sqrt{3}$). As a result, the number of flow-induced nuclei as found from Equation (19) increases faster at the free surface. Therefore, the lengthwise propagation of shish is higher at the free surface, resulting in a distribution of the total crystalline

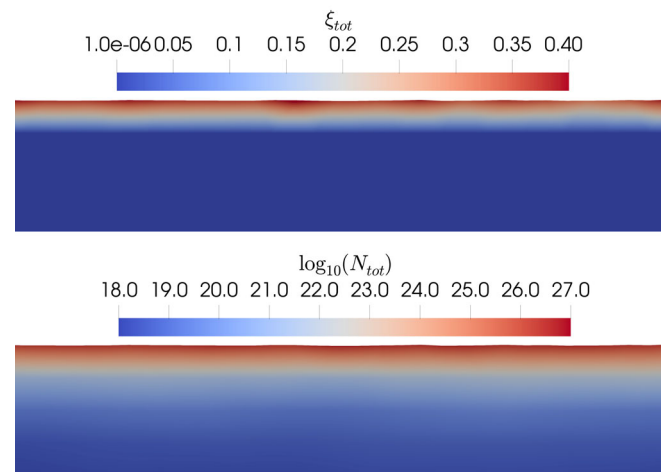


FIGURE 4 Space filling and nucleation distribution over the middle of the sample at a Hencky strain of $\epsilon_H = 5$. The compressed aspect ratio, strain rate and temperature are $\Lambda_c = 0.29$, $\dot{\epsilon} = 10 \text{ s}^{-1}$ and $T_0 = 140^\circ\text{C}$. The observed part of the sample has a length of 0.75 mm and mid-radius of $R = 0.15 \text{ mm}$. The free surface is positioned at the top of each figure and the center of the filament ($r = 0 \text{ mm}$) is positioned at the bottom

volume fraction and space filling over the radius of the sample (at $z = 0$ mm). In Figure 5, also the magnitude of orientation, $\text{tr}(\mathbf{c}_{\text{avg}})$ is visualized. This orientation parameter is used in the growth rate of alpha parents (see Equation (33)) which is affected by the distribution of strain rates. Eventually, this also affects the distribution of crystallization fraction.

Before crystallization, the temperature at the center of the sample and at the free surface are almost the same (see Figure 5). But after crystallization, due to the rapid increase in crystallization at the free surface, the temperature of the sample is increased according to Equation (6) and therefore the temperature also shows a distribution over the mid-radius of the filament. Since before crystallization the

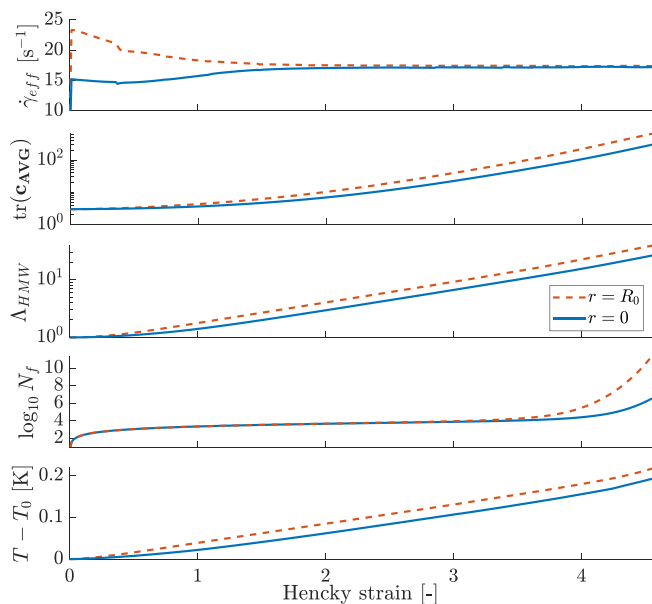
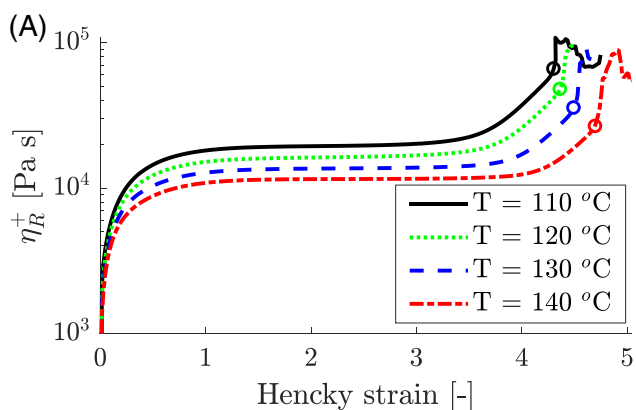


FIGURE 5 Important parameters for crystal growth at strains before crystallization (for $\langle \chi_{\text{tot}} \rangle < 10^{-5}$) at a strain rate and temperature of $\dot{\epsilon} = 10^5 \text{ s}^{-1}$ and $T_0 = 140^\circ\text{C}$. The used compressed aspect ratio is $\Lambda_c = 0.29$



temperature gradients are small, it can be concluded the effect of temperature gradients throughout the sample on the onset of crystallization is negligible. Hence, the crystallization kinetics are not affected by the temperature gradients before the onset of crystallization.

4.2 | Effect of experimental parameters

One of the goals of this study is to analyze the effect of relevant experimental parameters on crystallization in a FiSER. The effects of the applied strain rate and temperature on the crystallization of iPP are investigated for the following range of strain rates and temperatures: $\dot{\epsilon} = [0.71, 1.71, 4.14, 10] \text{ s}^{-1}$ and $T = [110, 120, 130, 140]^\circ\text{C}$. The resulting extensional viscosities are shown in Figure 6.

The extensional viscosity decreases with increasing temperature and strain rate, as expected for nonlinear rheology of a polymer melt.⁴⁶ When looking at the onset of crystallization, indicated by the markers in Figure 6, it can be seen that the strain at which crystallization starts becomes higher if the temperature increases. On the other hand, an increase in strain rate, decreases the strain at which crystallization starts. In Figure 7, the average crystallization is plotted versus the Hencky strain for the different experimental conditions. The critical crystallization strain is indicated by a circular marker. It can be seen that the critical crystallization strains are not the same for a strain rate range of $0.71 < \dot{\epsilon} < 10^5 \text{ s}^{-1}$ but they depend on both the strain rate and temperature. By comparing Figure 6 with Figure 7 it is concluded that the strain at which the second step upswing in extensional viscosity starts, matches the critical crystallization strain. This applies for all the simulations done here.

In an attempt to quantify this onset of crystallization, the critical crystallization strain $\epsilon_c(T, \dot{\epsilon})$ was introduced by Bischoff White et al.¹¹ This strain is defined as the strain at which a sudden increase of flow-induced crystallization fraction is observed (i.e., a steep increase in extensional viscosity). They found that for small strain rates a constant critical crystallization strain exists for iPP at $T = 146^\circ\text{C}$. In their

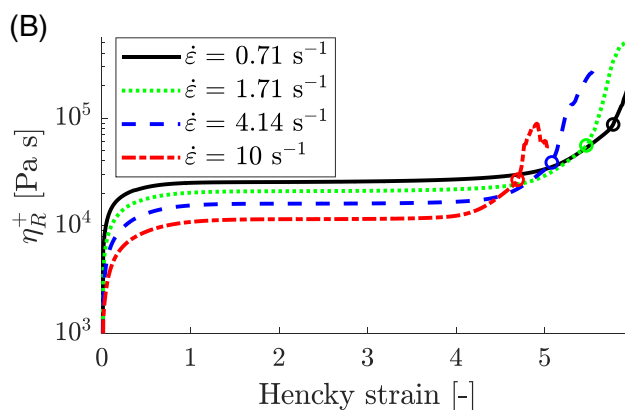


FIGURE 6 (a) Simulated extensional viscosity for the different values of the initial temperature. A strain rate of 10 s^{-1} is applied. (b) Simulated extensional viscosity for the different values of the strain rate. The initial temperature was set to 140°C . The markers indicate the onset of crystallization at each experimental condition. The used compressed aspect ratio is $\Lambda_c = 0.29$

measurements, no radius-based controller was used, but an exponential velocity profile was imposed on the pistons instead, that is, the length of the fluid filament is changed according to a constant exponential profile $L(t) = L_0 \exp(\dot{\epsilon}t)$. The resulting extension rate can then be calculated from the radius decay and shows to be higher than the applied strain rate and not constant. For an applied strain rate range of $0.01 < \dot{\epsilon} < 0.15 \text{ s}^{-1}$ they found that the critical crystallization strain for iPP is $\epsilon_c = 5.8$.¹¹ This value matches the values found here at

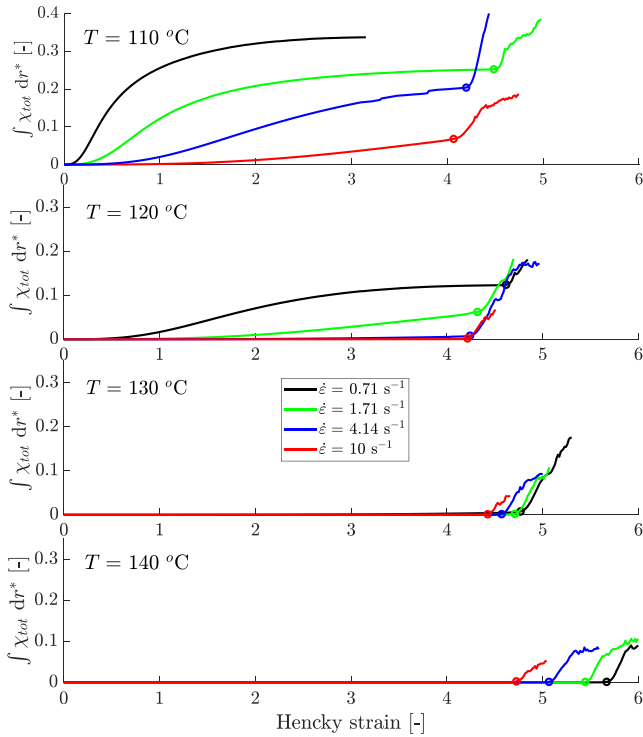


FIGURE 7 Average crystallinity for the different experimental conditions, with a compressed aspect ratio of $\Lambda_c = 0.29$. The markers indicate the critical crystallization strain ϵ_c at each experimental condition

$T = 140^\circ\text{C}$ for the lowest strain rate of 0.71 s^{-1} . However, it can be concluded from our simulations that no constant crystallization strain can be defined for iPP extended in the strain rate range of $0.71 < \dot{\epsilon} < 10 \text{ s}^{-1}$.

For an initial temperature of 110°C a significant increase of the average crystallinity is observed from the start (see Figure 7). This is a result of quiescent crystallization. At larger strains, the molecules are stretched to an extent that flow-induced crystallization also starts, resulting in a steep increase of the average crystallinity and extensional viscosity. For an initial temperature of 130 and 140°C no quiescent crystallization is observed, while for an initial temperature of 120°C , this depends on the applied strain rate (see Figure 7). For high strain rates, there is no time for the sample to show a quiescent crystalline contribution (at 120°C). Though the goal is to study flow-induced crystallization only, it is chosen to use all the data, because a clear distinction between quiescent and flow-induced crystallization can be seen. The fast increase in crystallinity in combination with the radius-based controller gives rise to numerical instabilities at the free surface. As a result of these instabilities, the velocity of the pistons is controlled in such a way that nonphysical jumps arise in the extensional viscosity and average crystallinity as shown in Figures 6 and 7. However, the simulation is stable for Hencky strains of 0.15–0.25 after the onset of crystallization, which allows studying crystallization in this strain range. The simulations with the experimental conditions of 110°C and 0.71 s^{-1} shows a rapid increase in crystallinity due to quiescent crystallization. This also gives rise to numerical instabilities and hence it was not possible to reach the onset of flow-induced crystallization for this experimental condition.

An overview of the dependency of the critical crystallization strain on the different experimental conditions is given in Figure 8. From this figure, two general trends follow. First, the critical crystallization strain is increasing with increasing temperature. Second, the critical crystallization strain is decreasing with increasing strain rate. Both trends cannot be explained by a simple shift function, because of the complex interplay between rheology and flow-induced

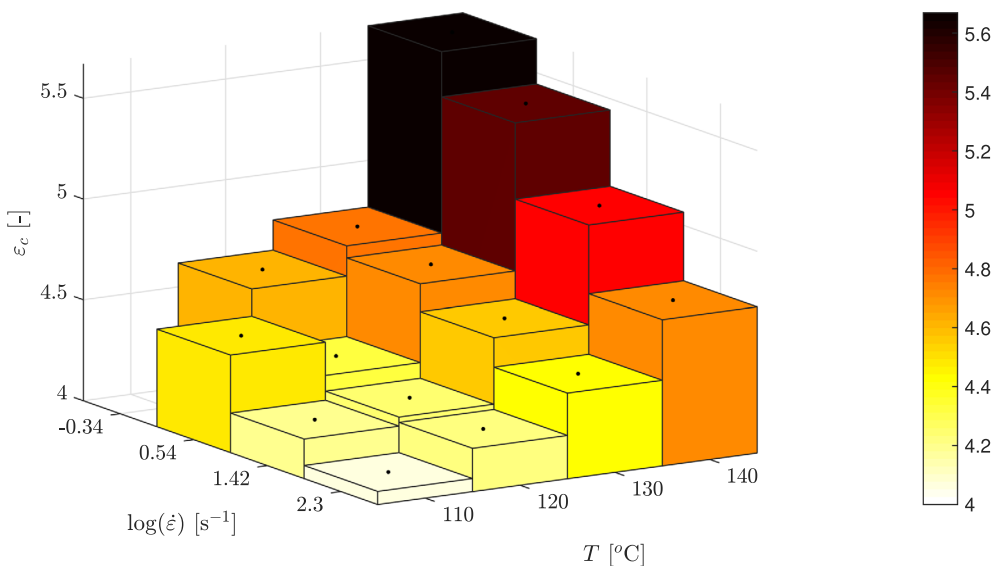


FIGURE 8 Dependency of critical crystallization strain on the strain rate and temperature for a sample with a compressed aspect ratio of $\Lambda_c = 0.29$. The natural logarithm of the strain rates are used, which correspond to strain rates of $\dot{\epsilon} = 0.71, 1.71, 4.14$ and 10 s^{-1} , respectively

crystallization. However, qualitatively a decrease of the critical crystallization strain when lowering the temperature is indeed expected since both nucleation density and growth rate increase at lower temperatures (Equations (13) and (14)). Moreover, at the same strain rate, a lower temperature will result in a larger molecular stretch. When considering the strain rate, the increased molecular stretch has enhancing effects on the flow-induced nucleation (Equation (19)), shish (Equation (24)) and kebab (Equation (33)) growth thereby resulting in a more than proportional reduction of the critical time for crystallization. It should be noted that the critical crystallization strains at $T = 110^\circ\text{C}$ are affected by quiescent crystallization. This can be seen by the fact that the crystallization starts at small strains, that is, at a weak flow (see Figure 7). This is also true for the strain rate of 0.71 s^{-1} and 1.71 s^{-1} at $T = 120^\circ\text{C}$. In Figure 8, it can be seen that the critical crystallization strain at $T = 110^\circ\text{C}$ and $\dot{\epsilon} = 1.71\text{ s}^{-1}$ (or $\log(\dot{\epsilon}) = 0.54\text{ s}^{-1}$) is inconsistent with the general trend. The other simulations, which are less affected by quiescent crystallization, are consistent with the pure flow-induced crystallization simulations.

4.3 | Dependency of crystallization on the aspect ratio

Since the nonhomogeneous flow at the start of filament stretching seems to affect the flow-induced crystallization, the dependency of crystallization on the aspect ratio is studied. Spiegelberg et al.¹⁷ showed that for increasing initial aspect ratio the flow near the middle of the filament converges to the desired pure uniaxial flow profile, that is, the effect of the end-plates reduces. To investigate whether this reduces the crystallization distribution over the mid-radius of the sample, the geometries in Table 1 are simulated at a strain rate of 10 s^{-1} at 130 and 140°C . A strain rate of 10 s^{-1} is chosen because it has the shortest simulation time of the strain rates used in this study. At the chosen temperatures, quiescent crystallization is negligible and therefore only flow-induced-crystallization occurs.

In Figure 9, the distribution of the crystallinity over the radius for geometry 2 (upper) and 4 (bottom) is given. These geometries have a

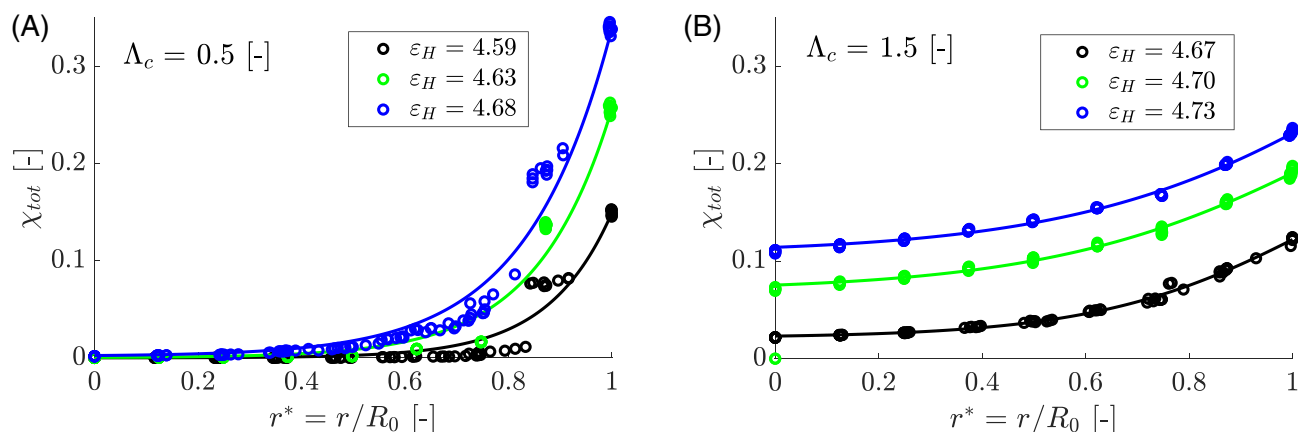


FIGURE 9 Crystallinity distributions for geometries 2 and 4 simulated at a strain rate of 10 s^{-1} and a temperature of 130°C . A) Compressed aspect ratio of $\Lambda_c = 0.5$. B) Compressed aspect ratio of $\Lambda_c = 1.5$. The lines are a guide for the eye

compressed aspect ratio of $\Lambda_c = 0.5$ and $\Lambda_c = 1.5$, respectively. It can be seen that the distribution of crystallinity is indeed affected by the initial dimensions of the sample. For a higher aspect ratio, using the same prestretch, the difference in crystallinity over the radius of the sample is reduced. In other words, the amount of crystallinity at the free surface is close to that at the center of the sample. For the geometry used in Figure 9B ($\Lambda_c = 1.5$), although an initial aspect ratio of $\Lambda_0 = 8.9$ is used, there still is a clear distribution of crystallinity over the mid-radius of the sample.

For the geometries in Table 1, the corresponding critical crystallization strains are given in Figure 10 for a strain rate of $\dot{\epsilon} = 10\text{ s}^{-1}$ and temperature of 130 and 140°C . The critical crystallization strain seems to converge when increasing the aspect ratio at both temperatures. This is as expected, because the flow converges to a pure uniaxial flow field at the middle of the sample when increasing the aspect ratio. However, because of the pistons there will always be a distribution of strain rates over the mid-filament and thereby a distribution of the onset of crystallization. Nevertheless, from upon a compressed aspect ratio of $\Lambda_c = 1.5$ ($\epsilon_{pre} = 1.74$, so $\Lambda_0 = 8.9$), the onset strain for crystallization will only slightly increase with Λ_c . For pure rheological measurements a much lower prestretch is required to measure the (pure uniaxial) extensional viscosity. From another work, currently under preparation, it follows that for a sample with $\epsilon_{pre} = 0.8$ and $\Lambda_0 = 2.5$, the error due to nonhomogeneous flow on the extensional viscosity is less than 5%. Therefore, the sample dimensions are even

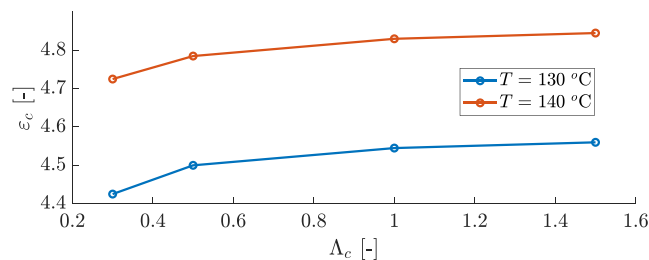


FIGURE 10 Critical crystallization strain versus the compressed aspect ratio ($\dot{\epsilon} = 10\text{ s}^{-1}$)

more important for in situ crystallization measurements in a FiSER. Since increasing the compressed aspect ratio from 0.29 to 1.5 only increases the onset of crystallization with about 2%, it can be concluded that the critical strain increase due to experimental parameters is only slightly affected by the initial geometry. Hence, the results in Figures 6-8, can be assigned to the complex interplay between flow, rheology and flow-induced crystallization.

To quantify the effect of the aspect ratio on crystallization, the simulated average crystallinity is plotted for different aspect ratios in Figure 11. As mentioned earlier, the critical crystallization strain depends on the aspect ratio. Therefore, the critical strain is subtracted from the Hencky strain, resulting in a strain definition that is only relevant in the flow-induced crystallization regime. For small aspect ratios, the crystallinity only grows near the free surface, and hence the integrated average crystallinity is small compared to large initial aspect ratios (see Figure 11). As strain increases, the center of the sample does not crystallize immediately for small aspect ratios, while for larger aspect ratios the crystallization rapidly increases over the total radius of the sample. Therefore, the rate of crystallization is lower for small sample aspect ratios, as can be seen in Figure 11. Unfortunately, the simulations become unstable at some Hencky strain after the onset of crystallization and therefore complete crystallization can not be reached numerically. Nevertheless, a clear relation between the aspect ratio and the onset of crystallization is shown. Besides, an increase in aspect ratio results in less distribution of crystallinity over the middle of the sample. From these findings, it can be concluded that an initial aspect ratio determines the distribution in crystallinity at large strains, due to the nonhomogeneous flow history. So to limit the crystallization distributions over the radius of the sample, the non-homogeneous flow at the start should become more homogeneous. Here, the approach of increasing the initial aspect ratio is followed, while it is also possible to decrease the piston diameter with strain⁴⁷ or to reshape the initial sample in a dog-bone geometry (like in tensile tests). This latter solution results in a more cylindrical profile and hence reduces the distribution of strain rates over the radius of the sample. Our numerical model can be used to study the flow and structure formation in such a dog-bone sample and to determine the optimal initial dog-bone geometry for uniaxial extensional flows and resulting crystallinity in a FiSER.

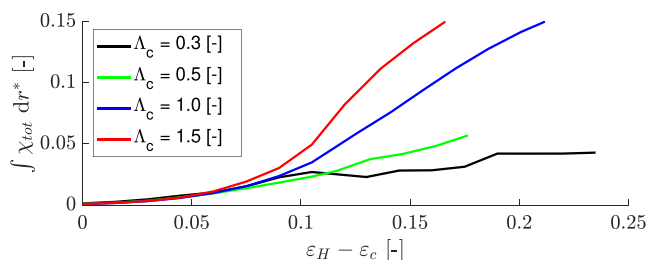


FIGURE 11 Average crystallinity for different aspect ratios at an initial temperature of $T = 130^{\circ}\text{C}$ and a strain rate of 10 s^{-1} . The strain axis is shifted with critical crystallization strain to match the onset of crystallization of the simulations

5 | CONCLUSIONS

A numerical model, describing the flow and resulting rheology and crystal structure development of iPP in a FiSER, is presented. In particular, finite element simulations are used that simultaneously solve the balance of mass, momentum and energy, a nonlinear viscoelastic constitutive (XPP) model and the equations for quiescent and flow-induced crystallization. A broad range of experimental parameters have been investigated by varying the initial temperature, the applied strain rate and the sample aspect ratio. From the simulations it follows that the extensional viscosity increases in steps. The first increase is due to the increase of the Rouse relaxation times during flow as a result of the increase of the amount of nuclei during flow, which are assumed to act as physical cross-links. The second step increase is a result of crystal growth, which causes a sharp increase in the moduli. Subsequently, the onset of crystallization in the FiSER has been investigated. While Bischoff White et al.¹¹ found a constant critical crystallization strain at low strain rates, this is not the case for the cases we studied for a strain rate range of $0.71 \leq \dot{\epsilon} \leq 10^5\text{ s}^{-1}$. Namely, the critical crystallization strain decreases with increasing strain rate. Besides, an increase in temperature increases the critical crystallization strain. These dependencies can be rationalized based on the effects of flow rate and temperature on rheology as well as nucleation and crystal growth. In addition, due to the nonhomogeneous flow, the molecular stretch is nonhomogeneously distributed over the radius of the filament. Before crystallization, the shear contributions at the pistons affect the flow in such a way that no pure uniaxial extensional flow is present in the FiSER. The molecular stretch determines the amount of flow-induced nuclei, which affects the onset of crystallization. As a result of the molecular stretch distribution, the crystallinity near the free surface is much higher than the crystallinity at the center of the sample, resulting in a distribution of crystallinity over the radius of the sample. Because the shear contributions at the pistons depend on the initial aspect ratio, the distribution of crystallinity can be reduced by increasing the initial aspect ratio. Other suggestions for reducing the molecular stretch distribution are decreasing the diameter of the pistons during flow⁴⁷ and reshaping the initial geometry to a dog-bone shape (as in tensile tests). In the future, this numerical model can be readily applied to optimize this initial dog-bone geometry and to investigate its effect on the flow and crystal structure formation in a FiSER. Thereby, the access to the local flow history allows us to account for nonidealities when analyzing results.

ACKNOWLEDGMENTS

The authors thank Dr. Martien A. Hulsen at the Eindhoven University of Technology, Eindhoven, the Netherlands for the access to the Toolkit for Finite Element Method (TFEM) software libraries.

AUTHOR CONTRIBUTIONS

This study was part of the MSc graduation project of Frank P.A. van Berlo. He was responsible for developing the computational model and for performing simulations and data analysis. He was supervised by Ruth Cardinaels, who also contributed to interpretation of the

results. Parts of the computational model originate from a capillary breakup rheometry (CaBER) model developed by Patrick D. Anderson. Ruth Cardinaels, Gerrit W. M. Peters and Patrick D. Anderson contributed to the critical revision of the article.

ORCID

Frank P. A. van Berlo  <https://orcid.org/0000-0002-1410-5458>

Ruth Cardinaels  <https://orcid.org/0000-0002-4191-6504>

Gerrit W. M. Peters  <https://orcid.org/0000-0001-7208-5128>

Patrick D. Anderson  <https://orcid.org/0000-0001-9157-0858>

REFERENCES

- [1] A. Keller, *Faraday Discuss. Chem. Soc.* **1979**, *68*, 145. <http://doi.org/10.1039/dc9796800145>.
- [2] A. Keller, H. W. H. Kolnaar, *Flow-Induced Orientation and Structure Formation*. Baden-Württemberg, Germany: VCH Verlagsgesellschaft mbH, **1997**.
- [3] G. Eder, H. Janeschitz-Kriegl, *Structure Development During Processing: Crystallization*. Baden-Württemberg, Germany: VCH Verlagsgesellschaft mbH, **1997**, p. 187.
- [4] C. Hadinata, D. Boos, C. Gabriel, E. Wassner, M. Rüllmann, N. Kao, M. Laun, *J. Rheol.* **2007**, *51*, 195. <http://doi.org/10.1122/1.2426977>.
- [5] A. J. McHugh, R. K. Guy, D. A. Tree, *Colloid Polym. Sci.* **1993**, *271*, 629. <http://doi.org/10.1007/BF00652825>.
- [6] D. J. Blundell, A. Mahendrasingam, C. Martin, W. Fuller, *J. Mater. Sci.* **2000**, *35*, 5057, 1004827630847. <http://doi.org/10.1023/A>.
- [7] F. H. M. Swartjes, G. W. M. Peters, S. Rastogi, H. E. H. Meijer, *Int. Polym. Process.* **2003**, *18*, 53. <http://doi.org/10.3139/217.1719>.
- [8] H. Janeschitz-Kriegl, *Colloid Polym. Sci.* **2003**, *281*, 1157. <http://doi.org/10.1007/s00396-002-0747-3>.
- [9] M. Sentmanat, O. Delgadillo-Velazquez, S. G. Hatzikiriakos, *Rheol. Acta* **2010**, *49*, 931. <http://doi.org/10.1007/s00397-010-0461-x>.
- [10] M. Chellamuthu, D. Arora, H. Winter, J. Rothstein, *J. Rheol.* **2011**, *55*, 901. <http://doi.org/10.1122/1.3593471>.
- [11] E. E. Bischoff White, H. Winter, J. Rothstein, *Rheol. Acta* **2011**, *51*, 303. <http://doi.org/10.1007/s00397-011-0595-5>.
- [12] S. L. Wingstrand, M. van Drongelen, K. Mortensen, R. S. Graham, Q. Huang, O. Hassager, *Macromolecules* **2017**, *50*, 1134. <http://doi.org/10.1021/acs.macromol.6b02543>.
- [13] S. L. Wingstrand, L. Imperiali, R. Stepanyan, O. Hassager, *Polymer* **2018**, *136*, 215. <http://doi.org/10.1016/j.polymer.2017.12.042>.
- [14] Y. Liu, W. Zhou, K. Cui, N. Tian, X. Wang, L. Liu, L. Li, Y. Zhou, *Rev. Sci. Instrum.* **2011**, *82*, 045104. <http://doi.org/10.1063/1.3574219>.
- [15] Z. Wang, F. Su, Y. Ji, H. Yang, N. Tian, J. Chang, L. Meng, L. B. Li, *J. Rheol.* **2017**, *61*, 589. <http://doi.org/10.1122/1.4982703>.
- [16] Z. Wang, J. Ju, L. Meng, N. Tian, J. Chang, H. Yang, Y. Ji, F. Su, L. Li, *Soft Matter* **2017**, *13*, 3639. <http://doi.org/10.1039/C7SM00107J>.
- [17] S. Spiegelberg, D. C. Ables, G. McKinley, *J. Non-Newtonian Fluid Mech.* **1996**, *64*, 229. [http://doi.org/10.1016/0377-0257\(96\)01439-5](http://doi.org/10.1016/0377-0257(96)01439-5).
- [18] J. Pepe, L. C. Cleven, E. J. M. C. Suijkerbuijk, E. C. A. Dekkers, D. Hermida-Merino, R. Cardinaels, G. W. M. Peters, P. D. Anderson, *Rev. Sci. Instrum.* **2020**, *91*, 073903. <https://doi.org/10.1063/5.0008224>.
- [19] H. Zuidema, G. W. M. Peters, H. E. H. Meijer, *Macromol. Theory Simul.* **2001**, *10*, 447. <http://doi.org/10.1002/1521-3919>.
- [20] R. J. A. Steenbakkens, G. W. M. Peters, *J. Rheol.* **2011**, *55*, 401. <http://doi.org/10.1122/1.3545844>.
- [21] T. B. van Erp, P. C. Roozmond, G. W. M. Peters, *Macromol. Theory Simul.* **2013**, *22*, 309. <http://doi.org/10.1002/mats.201300004>.
- [22] M. van Drongelen, P. C. Roozmond, E. M. Troisi, A. K. Doufas, G. W. M. Peters, *Polymer* **2015**, *76*, 254. <https://doi.org/10.1016/j.polymer.2015.09.010>.
- [23] F. J. M. F. Custódio, R. Steenbakkens, P. D. Anderson, G. W. M. Peters, H. E. H. Meijer, *Macromol. Theory Simul.* **2009**, *18*, 469. <https://doi.org/10.1002/mats.200900016>.
- [24] P. C. Roozmond, M. van Drongelen, Z. Ma, M. A. Hulsen, G. W. M. Peters, *J. Rheol.* **2015**, *59*, 613. <http://doi.org/10.1122/1.4913696>.
- [25] P. C. Roozmond, T. B. van Erp, G. W. M. Peters, *Polymer* **2016**, *89*, 69. <http://doi.org/10.1016/j.polymer.2016.01.032>.
- [26] G. Grosso, E. M. Troisi, N. O. Jaensson, G. W. M. Peters, P. D. Anderson, *Polymer* **2019**, *182*, 121806. <http://doi.org/10.1016/j.polymer.2019.121806>.
- [27] D. A. Nicholson, G. C. Rutledge, *J. Chem. Phys.* **2016**, *145*, 244903. <https://doi.org/10.1063/1.4972894>.
- [28] L. Zhao, Y. Hu, Y. Shao, Z. Liu, B. Liu, X. He, *J. Chem Phys.* **2019**, *150*, 184114. <https://doi.org/10.1063/1.5089694>.
- [29] M. H. Nafar Sefiddashti, B. Edwards, B. Khomami, *Macromolecules* **2020**, *53*, 6432. <https://doi.org/10.1021/acs.macromol.0c00508>.
- [30] D. J. Read, C. Mclroy, C. Das, O. G. Harlen, R. S. Graham, *Phys. Rev. Lett.* **2020**, *124*, 147802. <https://doi.org/10.1103/PhysRevLett.124.147802>.
- [31] J. Housmans, M. Gahleitner, G. W. M. Peters, H. E. H. Meijer, *Polymer* **2009**, *50*, 2304. <http://doi.org/10.1016/j.polymer.2009.02.050>.
- [32] P. C. Roozmond, Z. Ma, K. Cui, L. Li, G. W. M. Peters, *Macromolecules* **2014**, *47*, 5152. <http://doi.org/10.1021/ma501108c>.
- [33] W. M. H. Verbeeten, G. W. M. Peters, F. P. T. Baaijens, *J. Non-Newtonian Fluid Mech.* **2004**, *117*, 73. <http://doi.org/10.1016/j.jnnfm.2003.12.003>.
- [34] W. M. H. Verbeeten, G. W. M. Peters, F. P. T. Baaijens, *J. Rheol.* **2001**, *45*, 823. <http://doi.org/10.1122/1.1380426>.
- [35] W. Schneider, A. Köppl, J. Berger, *Int. Polym. Process.* **1988**, *2*, 151. <http://doi.org/10.3139/217.880150>.
- [36] L. Fernandez-Ballester, D. W. Thurman, W. Zhou, J. A. Kornfield, *Macromolecules* **2012**, *45*, 6557. <http://doi.org/10.1021/ma3000384>.
- [37] C. Geuzaine, J.-F. Remacle, *Int. J. Numerical Methods Eng.* **2009**, *79*, 1309. <http://doi.org/10.1002/nme.2579>.
- [38] C. Balemans, M. A. Hulsen, P. D. Anderson, *Appl. Sci.* **2017**, *7*, 516. <https://doi.org/10.3390/app7050516>.
- [39] C. Balemans, N. O. Jaensson, M. A. Hulsen, P. D. Anderson, *Addit. Manuf.* **2018**, *24*, 528. <https://doi.org/10.1016/j.addma.2018.09.005>.
- [40] M. A. Hulsen, R. Fattal, R. Kupferman, *J. Non-Newtonian Fluid Mech.* **2005**, *127*, 27. <http://doi.org/10.1016/j.jnnfm.2005.01.002>.
- [41] A. N. Brooks, T. J. R. Hughes, *Comput. Methods Appl. Mech. Eng.* **1982**, *32*, 199. [http://doi.org/10.1016/0045-7825\(82\)90071-8](http://doi.org/10.1016/0045-7825(82)90071-8).
- [42] A. C. B. Bogaerds, A. M. Grillet, G. W. M. Peters, F. P. T. Baaijens, *J. Non-Newtonian Fluid Mech.* **2002**, *108*, 187. [https://doi.org/10.1016/S0377-0257\(02\)00130-1](https://doi.org/10.1016/S0377-0257(02)00130-1).
- [43] C. Hirt, A. Amsden, J. Cook, *J. Comput. Phys.* **1974**, *14*, 227. [http://doi.org/10.1016/0021-9991\(74\)90051-5](http://doi.org/10.1016/0021-9991(74)90051-5).
- [44] N. O. Jaensson, M. A. Hulsen, P. D. Anderson, *Comp. Fluids* **2015**, *111*, 1. <http://doi.org/10.1016/j.compfluid.2014.12.023>.
- [45] G. D'Avino, M. A. Hulsen, P. L. Maffettone, *Comput. Fluids* **2012**, *66*, 183. <http://doi.org/10.1016/j.compfluid.2012.06.023>.
- [46] R. B. Bird, *Annu. Rev. Fluid Mech.* **1976**, *8*, 13. <http://doi.org/10.1146/annurev.fl.08.010176.000305>.
- [47] S. Berg, R. Kröger, H. Rath, *J. Non-Newtonian Fluid Mech.* **1994**, *55*, 307. [https://doi.org/10.1016/0377-0257\(94\)80075-8](https://doi.org/10.1016/0377-0257(94)80075-8).

How to cite this article: van Berlo FPA, Cardinaels R, Peters GWM, Anderson PD. A numerical study of extensional flow-induced crystallization in filament stretching rheometry. *Polymer Crystallization*. 2021;4:e10154. <https://doi.org/10.1002/pcr2.10154>

APPENDIX: MATERIAL CHARACTERIZATION A.

Here, the material parameters of the iPP homopolymer (Borealis HD601CF) are given. The relaxation spectra and nonlinear parameters used in the XPP constitutive relation are given in Table A.1.

TABLE A1 Viscoelastic model parameters of the XPP model for iPP at a reference temperature of 220°C as derived by Grosso et al.²⁶

N_{modes}	η_i (Pa s)	$\lambda_{b,i}$ (s)	$\lambda_{s,i}$ (s)	ν_i (-)
1	30.00	$5 \cdot 10^{-5}$	$6.00 \cdot 10^{-6}$	0.05
2	130.76	0.0014	$6.67 \cdot 10^{-6}$	0.05
3	303.60	0.011	$5.24 \cdot 10^{-5}$	0.05
4	480.00	0.060	$2.86 \cdot 10^{-4}$	0.05
5	377.00	0.29	0.0014	0.05
6	183.70	1.67	0.0080	0.05
7	46.00	11.5	0.055	0.017

In Table A.4, the crystallization parameters are given which are used in the numerical simulations.

Nucleation density					
N_{ref}	$2.2 \cdot 10^{15}$			1/m ³	
$T_{N,\text{ref}}$	383			K	
c_N	0.211			1/K	
Crystal growth		α -phase	β -phase	γ -phase	
$G_{\text{max},0}$	$19.2 \cdot 10^{-6}$	$7.1 \cdot 10^{-6}$	$4.4 \cdot 10^{-6}$		m/s
$T_{G,\text{ref},0}$	363	380	377		K
c_G	$2.3 \cdot 10^{-3}$	$6.6 \cdot 10^{-3}$	$3.5 \cdot 10^{-3}$		1/K
FIC					
f_β	0.002			-	
$g_{n,\text{ref}}$	10^{13}			1/(m ³ s)	
$c_{n,T}$	-0.016			1/K	
μ_n	0.015			-	
ξ_{seg}	$5 \cdot 10^{-9}$			m	
G_{flow}	0.009			-	
Effect on rheology					
r_{eff}	$30 \cdot 10^{-6}$			m	
μ	5			-	
T_{ref}	493			K	
E_a	$40 \cdot 10^3$			J/mol	
α_s	10^{-13}			m ³	

Material parameters used in the heat balance are given in Table A.2.

TABLE A2 Material parameters used for the heat balance²⁴

	ρ kg/m ³	c_p J/(kg K)	k W/(m K)	χ_∞ -	ΔH J/g
iPP	800	3157	0.11	0.650	207
steel	8000	670	80	x	x

The parameters used for the boundary conditions are specified in Table A.3.

TABLE A3 Material parameters used for the boundary conditions

	$\dot{\gamma}_{24}$ mN/m	h W/(m ² K)
iPP	30.2	79

TABLE A4 Crystallization parameters for iPP as derived by Grosso et al.²⁶ using molecular considerations